

Design Aspects of an Active Electromagnetic Suspension System for Automotive Applications

Bart L. J. Gysen, *Student Member, IEEE*, Jeroen L. G. Janssen, *Student Member, IEEE*,
Johannes J. H. Paulides, *Member, IEEE*, and Elena A. Lomonova, *Senior Member, IEEE*

Abstract—This paper is concerned with the design aspects of an active electromagnetic suspension system for automotive applications which combines a brushless tubular permanent-magnet actuator with a passive spring. This system provides for additional stability and safety by performing active roll and pitch control during cornering and braking. Furthermore, elimination of the road irregularities is possible, hence, passenger drive comfort is increased. Based upon measurements, static and dynamic specifications of the actuator are derived. The electromagnetic suspension is installed on a quarter-car test setup, and the improved performance using roll control is measured and compared with a commercial passive system. An alternative design using a slotless external-magnet tubular actuator is proposed which fulfills the thermal and volume specifications.

Index Terms—Active suspension, optimization, permanent-magnet actuator.

I. INTRODUCTION

IN THE FUTURE, active suspension systems will replace conventional passive suspension systems since vehicle stability and passenger safety are high concerns for car designers. Cars tend to become smaller (SMART) and incorporate a higher center of gravity (SUV) and a reduced footprint, which increases the need for a suspension system with a rigid response when driving into turns while absorbing the road irregularities when driving under low-yaw circumstances (relatively straight). Currently, commercial systems consist of hydraulic or pneumatic actuators (for example, those installed on Citroen, Rolls-Royce, Mercedes Benz, etc.) which offer a high force density and ease in design due to the commercial availability of the various parts. However, these systems have a relatively low bandwidth (around 1 Hz) [1], [2] probably due to leakage in the valves and pressure hoses and limited bandwidth of the pump. Furthermore, these systems are inefficient due to the need for a continuous pressurized system. In general, electromagnetic suspension systems have a very small response time and are,

therefore, more suitable to absorb road vibrations and to react in lane-change maneuvers. An example of a commercial electromagnetic semiactive suspension system is the magnetorheological damper [3], [4], developed by Delphi Corporation (installed on Audi, Cadillac, Ferrari), which has the ability to change its damper characteristic within 1 ms [5]. However, since it is a semiactive system, no active force can be applied and, therefore, total roll and pitch elimination is impossible. This paper proposes an electromagnetic active suspension system comprising of a brushless tubular permanent-magnet actuator (TPMA) [6], [7], in parallel with a mechanical spring [8], [9]. These actuators have a relatively high force density due to the tubular structure and excellent servo characteristics with a bandwidth in excess of 50 Hz. Furthermore, electromagnetic actuators allow for bidirectional power flow and hence, both motor and generator modes are possible. The former is used to apply active forces on the sprung mass to eliminate roll and pitch movements, and the latter is used to absorb road vibrations and act as a damper where the absorbed power can be fed to the battery in order to supply auxiliary loads. Actuator-force specifications will be derived in Section II based upon vertical-acceleration measurements during a test drive on the Nürburgring. In Section III, the proof of principle will be shown by means of measurements on an in-house designed and built quarter-car test setup which mimics the roll behavior. Since a redesign of the total suspension is an expensive solution, this paper proposes a “plug and play” suspension system in Section IV, which means that the volume specifications are based upon the currently installed passive suspension systems for both low-voltage (general cars) and high-voltage applications (hybrid cars). A slotless TPMA is proposed in Section V where it is shown that, by means of optimization, the inverted Halbach magnetized topology offers the highest force density.

II. SYSTEM SPECIFICATIONS

In order to design a suspension system capable of eliminating roll and pitch behavior, it is necessary to identify the forces acting on the unsprung and sprung mass. As an example, during fast cornering, centrifugal forces tend to roll the car around the roll axis which causes an unbalance of the load or a load transfer from the inner to the outer wheels.

In such an example, using Fig. 1, the vertical dynamic force on the tires can be calculated as [10]

$$F_{\text{dyn}} = (m_s + m_u)a_y \frac{h_{\text{CoG}}}{T} \quad (1)$$

Paper 2008-IDC-121.R1, presented at the 2008 Industry Applications Society Annual Meeting, Edmonton, AB, Canada, October 5–9, and approved for publication in the IEEE TRANSACTIONS ON INDUSTRY APPLICATIONS by the Industrial Drives Committee of the IEEE Industry Applications Society. Manuscript submitted for review October 31, 2008 and released for publication March 3, 2009. First published July 14, 2009; current version published September 18, 2009. This work was supported by SKF.

The authors are with the Department of Electrical Engineering, Eindhoven University of Technology, 5600 MB Eindhoven, The Netherlands (e-mail: B.L.J.Gysen@tue.nl; j.l.g.janssen@tue.nl; j.j.h.paulides@tue.nl; e.lomonova@tue.nl).

Color versions of one or more of the figures in this paper are available online at <http://ieeexplore.ieee.org>.

Digital Object Identifier 10.1109/TIA.2009.2027097

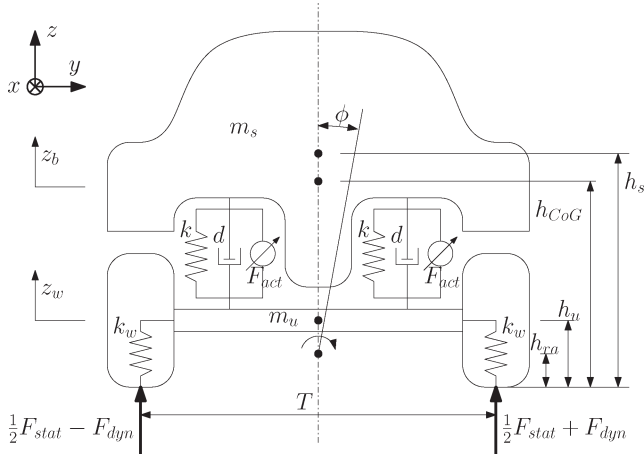


Fig. 1. Half-car model for calculation of the roll forces.

TABLE I
PARAMETERS OF THE TEST VEHICLE

Parameter	Value	Description
m_s	1613 kg	Sprung mass
m_{u_f}	96.6 kg	Front unsprung mass
m_{u_r}	89.8 kg	Rear unsprung mass
h_{CoG}	0.544 m	Center of gravity height
h_{ra}	8.98 cm	Roll axis height
h_u	0.31 m	Wheel axle height
T	1.57 m	Track width
ψ_m	50.9 %	Front/total mass ratio
γ_f	0.7	Front/total roll force distribution ratio
C_f	0.925	Front suspension force ratio
C_r	0.98	Rear suspension force ratio

where a_y is the centrifugal acceleration during cornering. The vertical forces exerted on the tires by the unsprung mass F_u and sprung mass F_s can be calculated as

$$\begin{aligned} \text{Front : } F_{u_f} &= m_{u_f} a_y \frac{h_u}{T} \\ F_{s_f} &= \psi_m m_s a_y \frac{h_{ra}}{T} \\ F_{act_f} &= \frac{1}{C_f} (\gamma_f F_{dyn} - F_{u_f} - F_{s_f}) \end{aligned} \quad (2)$$

$$\begin{aligned} \text{Rear : } F_{u_r} &= m_{u_r} a_y \frac{h_u}{T} \\ F_{s_r} &= (1 - \psi_m) m_s a_y \frac{h_{ra}}{T} \\ F_{act_r} &= \frac{1}{C_r} ((1 - \gamma_f) F_{dyn} - F_{u_r} - F_{s_r}) \end{aligned} \quad (3)$$

where m_{u_f} and m_{u_r} are the unsprung masses of the front and rear axle, respectively and ψ_m is the ratio of the total sprung mass acting on the front axle. Due to the independence of the actuators, it is possible to introduce a force ratio γ_f between the front and rear axle which gives the possibility to control for understeer compared with the more dangerous oversteer behavior. The force ratios C_f and C_r are introduced since the struts are not exactly vertically mounted. In order to calculate the actuator forces, the lateral acceleration a_y is measured during a one-lap test drive with a BMW 530 on the Nürburgring in Germany, and the actuator forces are calculated using the parameters given in Table I. A short interval of the actuator forces calculated from the measured lateral acceleration is

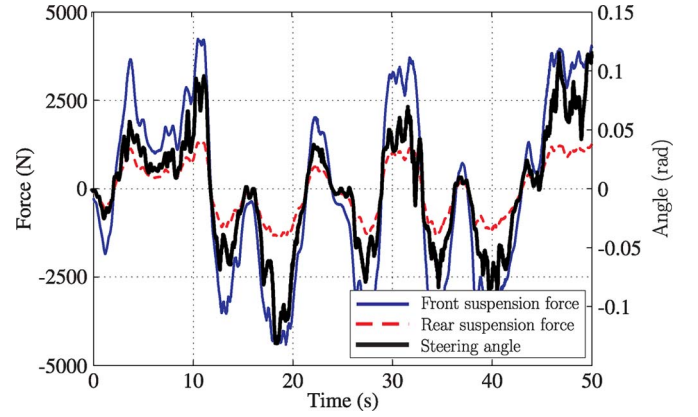


Fig. 2. Roll forces calculated from the measured lateral acceleration on the Nürburgring together with the measured steering angle.

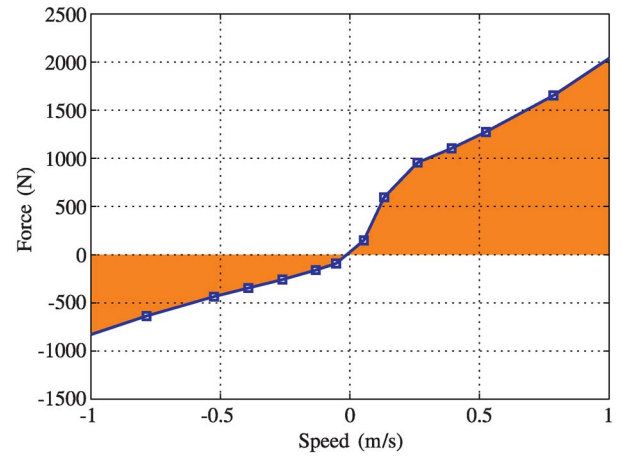


Fig. 3. Nominal damping characteristic of the passive damper and the working area for the active suspension.

shown in Fig. 2 together with the steering angle, where, to eliminate the roll angle and using the complete data set, a peak and rms forces of 4 and 2 kN, respectively, are derived for the front actuators. As a comparison, Martins *et al.* [11] showed that an rms force of 1050 N is necessary to achieve the “reduced-comfort boundary,” which is a 67% improvement compared with the standard ISO 2631 levels.

However, in general, passenger cars are not designed for continuously driving under these conditions, and it can be assumed that the previous derived force levels should be attained with a duty cycle of around 50%. The continuous force level is therefore assumed to be 1 kN for total roll and pitch elimination, with a peak force of 4 kN. Note that these force specifications are only necessary at low vertical speed (< 0.1 m/s).

Next to the roll and pitch requirements, the actuator should still be capable of delivering the required damping force; note that in this case, the actuator works in generator mode, and energy is subtracted from the system to drive auxiliary loads or to charge the battery. When a load is applied to the actuator due to road vibration, a voltage will be induced resulting in a current flow through a variable load, and therefore, a variable opposite force is applied against the vibration forces, and, hence, a variable damping effect is achieved. The actuator should be capable of handling the amount of current within the thermal constraints of the system. In Fig. 3, the measured damping

TABLE II
 SPECIFICATIONS OF THE SUSPENSION SYSTEM

Specification	Value	Description
$F_{\text{rms roll}}$	1000 N	Rms force at 0.1 m/s for active roll control
$F_{\text{max roll}}$	4000 N	Max. force at 0.1 m/s for active roll control
$F_{\text{rms damp}}$	762 N	Rms force at 1 m/s for active damping
$F_{\text{max damp}}$	2050 N	Max. force at 1 m/s for active damping
ΔT_{max}	80 °C	Maximum increase in temperature
v_{max}	1 m/s	Maximum speed
z_{max}	140 mm	Minimum stroke

characteristic of the passive damper is shown up to 1 m/s which is the maximum necessary damping speed indicated by the Verband der Automobilindustrie. The actuator should be capable of absorbing these damping forces. Furthermore, it is assumed that all speeds from -1 until 1 m/s occur with the same probability. Hence, an average of the absolute value of the nominal graph is a measure for the necessary continuous damping force, which is 762 N in this case, with a maximum force of 2.05 kN at 1 m/s (see Table II). Although the actuator only needs a short-stroke capability for roll and pitch behavior, it still needs a long stroke for absorbing the road irregularities. For this reason, the stroke specifications are comparable with the passive suspension system. As mentioned before, the volume specifications are such that the active suspension strut can replace the passive one without drastically changing the car design as will be discussed in Section IV. Regarding power constraints, the temperature increase of the actuator should be limited to 80 °C which means that together with an ambient temperature that can reach 40 °C, the actuator's actual temperature will not exceed 120 °C which is a standard limiting temperature in automotive engineering.

III. QUARTER-CAR TEST SETUP

In order to verify the increased performance of the electromagnetic suspension system, measurements are performed on a quarter-car test setup. Although roll and pitch are a coupled behavior, they can be modeled as a disturbance force acting on each of the four corners of a vehicle. This simplification leads to the ability of decoupling each corner of the car, resulting in a quarter-car model. During cornering and braking, it is assumed that the unsprung mass movement is relatively small and, therefore, wheel dynamics are neglected which simplifies the setup to a single moving quarter-car mass (see Figs. 4 and 5). Mimicking of cornering and braking will be performed by applying a body force F_{body} (see Fig. 6), of 1920 N to the quarter-car mass during a time interval which is typically around 3 s as obtained from the measurements on the Nürburgring. The duty cycle of applying this disturbance force is 50%, corresponding to an rms force of 960 N which is close to the specified 1 kN. An industrial brushless TPMA [12] is used, which does not satisfy volume, mass, and voltage constraints, but is still suitable to determine the functioning and performance of an electromagnetic suspension system.

In this setup, the position and speed of the quarter-car mass are measured with an optical triangulation sensor; however, in practice, not the displacement but the roll angle needs to

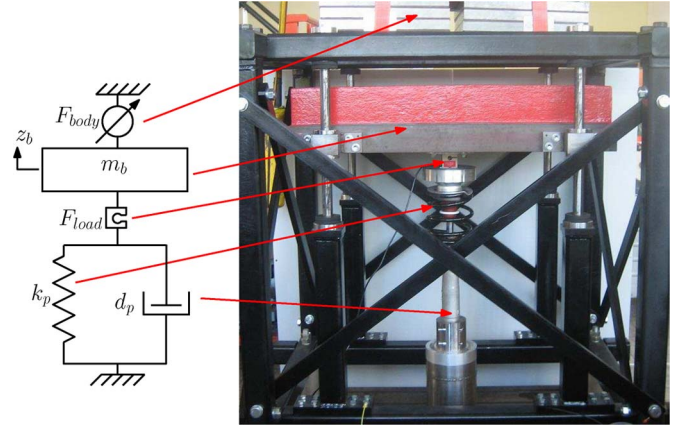


Fig. 4. Schematic view and illustration of the quarter-car test setup with a passive suspension.

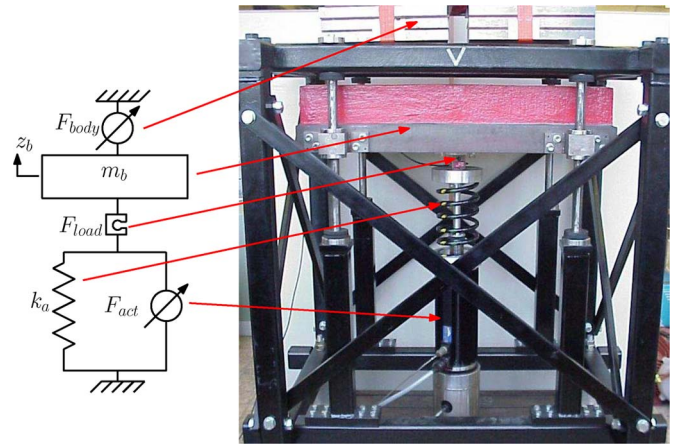


Fig. 5. Schematic view and illustration of the quarter-car test setup with an active electromagnetic suspension.

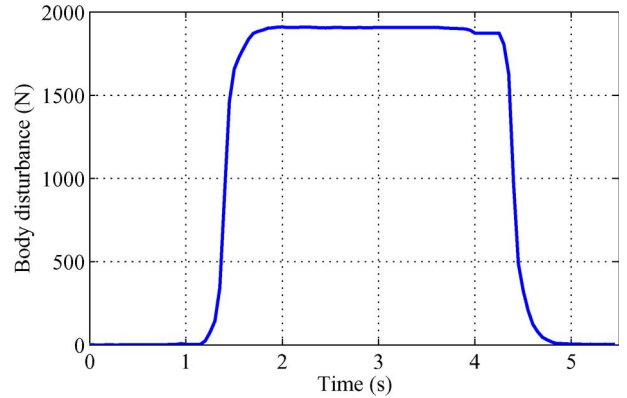


Fig. 6. Load profile of the body load applied to the quarter-car mass.

be measured. For this setup, the roll angle ϕ is related to the position of the sprung mass z_b as

$$\phi = \arctan \left(\frac{2z_b}{T} \right). \quad (4)$$

Furthermore, a force sensor is incorporated in order to identify the load profile of the applied body force. The control and signal processing are performed with Matlab-dSpace software and hardware where, depending on the proportional gain of the

TABLE III
PARAMETERS OF THE QUARTER-CAR TEST SETUP

Parameter	Value	Description
m_b	387 kg	Quarter car mass
k_p	29.1 kN/m	Spring constant of the passive suspension
d_p	see Fig. 3	Passive damper characteristic
k_a	31.2 kN/m	Spring constant of the active suspension
F_{body}	see Fig. 6	Body force

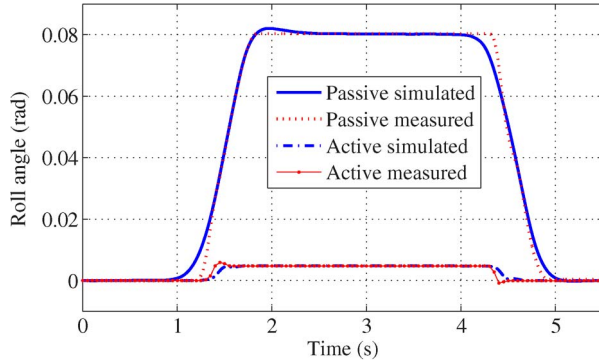


Fig. 7. Passive and active roll control measurements.

controller, the body displacement can be minimized at the expense of power consumption. The parameters of the setup are given in Table III. In Fig. 7, the simulated and measured responses of the passive and active suspension system on the body force are shown. It can be observed that the electromagnetic suspension system immediately reacts on the applied force, and the roll angle is minimized up to 5.9% of the passive roll angle. This provides for a tradeoff between the allowable roll and power consumption. For example, if zero body roll is obtained, no mechanical energy is produced, hence, speed-dependent losses can be neglected. The steepness of the actuator $S = F_{act}^2 / P_{cu}$, where P_{cu} are the copper losses, is $5790 \text{ N}^2/\text{W}$, and, hence, the power as function of the body force and roll angle ϕ can approximately be written as

$$P_{cu} \approx \frac{\left(F_{body} - \frac{k_a T \tan(\phi)}{2}\right)^2}{S}. \quad (5)$$

To achieve zero body roll, 636 W is necessary per wheel for the body disturbance of 1920 N. However, taking into account the specified duty cycle of 50%, the continuous power is 318 W per wheel. The used electromagnetic actuator has an active length of 364 mm and an outer diameter of 157 mm, hence, it is not suitable regarding the available space envelope in a BMW 530. Furthermore, the induced peak electromotive force (EMF) at 1 m/s is 126.7 V. Hence, the next section will discuss an alternative design of an actuator by means of an optimization routine with respect to the available space envelope and supply voltages.

IV. SUSPENSION DESIGN AND ACTUATOR CONSTRAINTS

A. Suspension Design

In Fig. 8(a), the passive suspension system is shown which consists of a mechanical spring in parallel with a passive hydraulic or pneumatic damper. The proposed electromagnetic

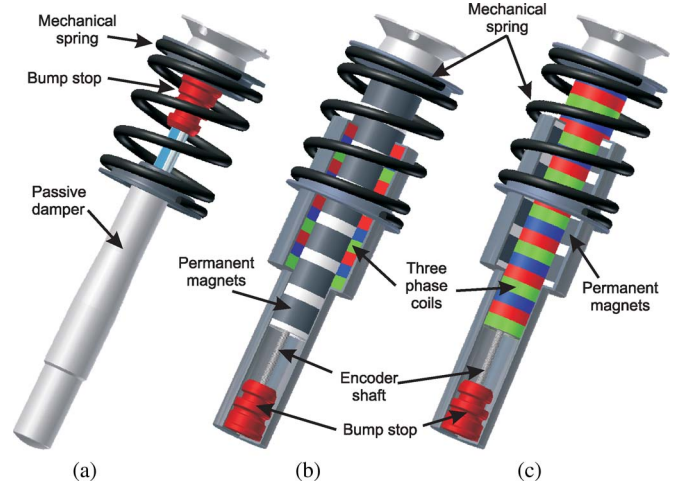


Fig. 8. Suspension struts. (a) Passive. (b) Active interior-magnet TPMA, (c) Active exterior-magnet TPMA.

active-suspension strut is shown in Fig. 8(b) and (c) which both consist of a slotless brushless three-phase TPMA in parallel with a mechanical spring. Due to the ease in modeling, design, and fabrication, the low-force ripples and low cost, a slotless TPMA is preferred over a slotted one. Two different topologies are considered for the actuator: interior and exterior magnet, as shown in Fig. 8(b) and (c), respectively, and the cross sections are shown in Fig. 9(a) and (b), respectively. The exterior-magnet topology offers the benefit of the absence of a cable slap; however, in order to keep the power level to a minimum, switching of coil sets should be implemented based upon position monitoring. Since this is also necessary for commutation in order to have a long-stroke movement, a linear encoder is embedded in the hollow shaft. The permanent magnets have a remanent flux density of 1.23 T and a relative recoil permeability of 1.05.

B. Volume and Mass Constraints

The active-suspension strut is designed to replace the passive one, and, as a result, the outer radius of the translator and the outer radius and length of the stator have an upper constraint. There is a minimum constraint on the radius of the hollow shaft since a linear encoder is embedded. The moving mass should be limited to 16 kg; however, considering the available volume, this is not a hard constraint and is therefore easily achieved. The housing of the strut is made of aluminum for its low weight, high thermal conductivity, and nonmagnetic properties.

C. Thermal Constraints

The design objective is to maximize the mean force within a constrained volume, hence, the actuator design always tends to have the maximum outer radius and axial length, and, if not, aluminum could be added in order to increase the heat convection and, hence, the performance. The air-gap length g is fixed to 1 mm to allow the use of sliding bearings, which increases the thermal conduction. The overall thermal behavior of the tubular actuator only moderately changes by varying the other geometrical parameters or magnetization pattern, hence,

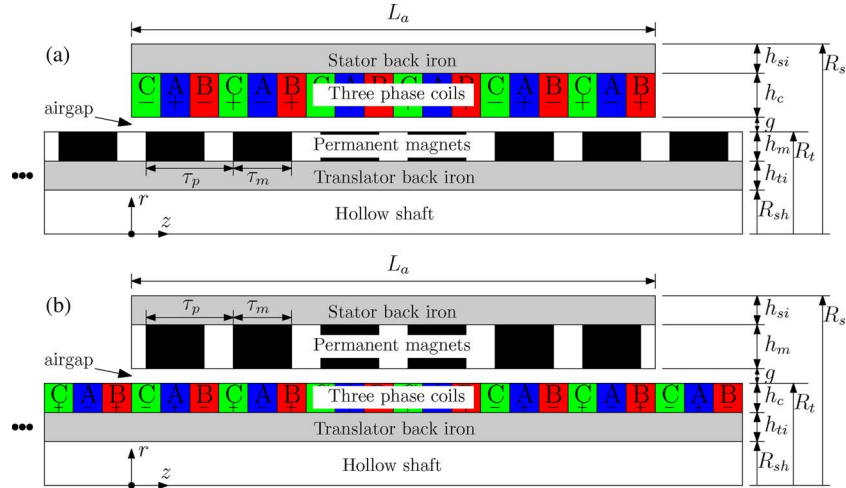


Fig. 9. Schematic view of slotless TPMA. (a) Interior magnet. (b) Exterior magnet.

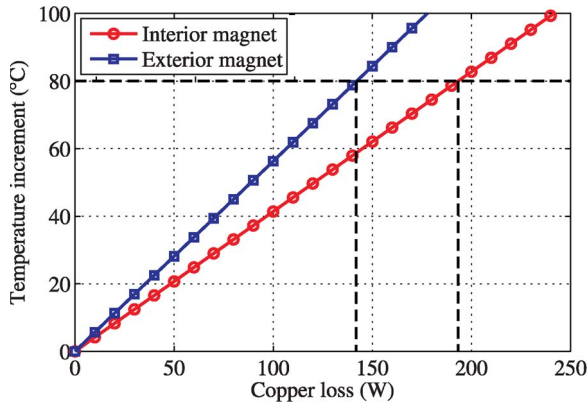


Fig. 10. Temperature increment of the actuator as function of the copper losses.

the maximum copper losses are obtained for a fixed maximum temperature rise of 80 °C. However, significant differences do arise when the topology is varied, i.e., interior- or exterior-magnet topology. Using a 2-D thermal finite-element model, the temperature distribution is calculated for both topologies. To illustrate the thermal behavior, the maximum actuator temperature is given as a function of the copper losses, as shown in Fig. 10. It can be observed that the maximum copper losses are 193 and 143 W for the interior- and exterior-magnet topology, respectively, for the maximum temperature rise of 80 °C. The exterior-magnet topology allows for less copper losses, since they have to travel through the air gap and magnet array before convection can occur. The total temperature distribution for the 80-°C temperature rise is shown in Fig. 11 for both topologies. Finally, a list of all the constraints is presented in Table IV.

V. ACTUATOR MODELING, OPTIMIZATION, AND DESIGN

A. Magnetostatic Design

In this section, an actuator design will be derived according to the specifications and constraints mentioned in the previous sections. Both interior- and exterior-magnet topologies are considered [see Fig. 9(a) and (b)], respectively, for three different

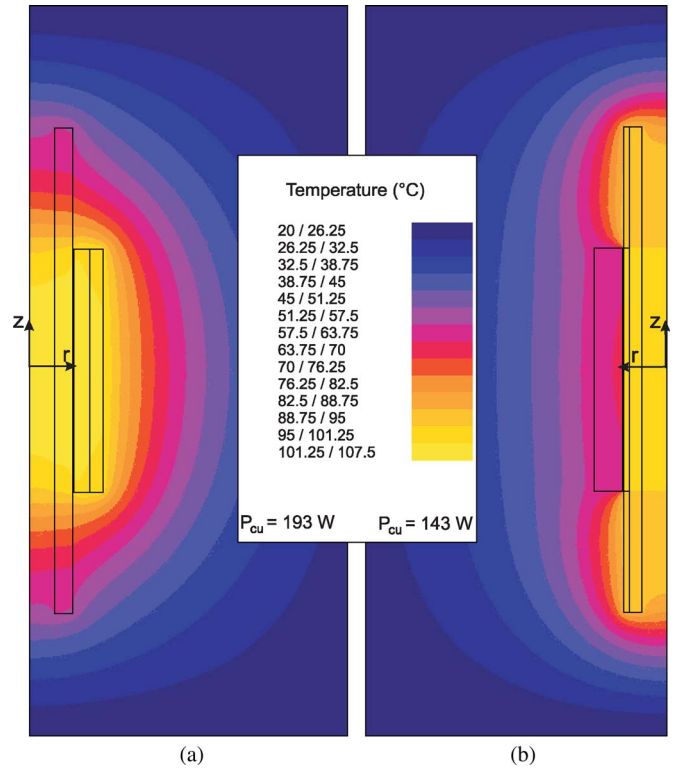


Fig. 11. Temperature distribution of (a) the interior-magnet topology and (b) the exterior magnet topology (Halbach magnetization).

 TABLE IV
ACTUATOR CONSTRAINTS

Constraint	Description
$L_a < 200$ mm	Length of the stator
$R_{sh} < R_t < 35$ mm	Radius of the translator
$R_t + g < R_s < 60$ mm	Radius of the stator
$R_{sh} > 20$ mm	Radius of hollow shaft
$P_{cu_i} < 193$ W	Copper losses for the interior magnet top.
$P_{cu_e} < 143$ W	Copper losses for the exterior magnet top.
$B_{iron} < 1.5$ T	Flux density in the iron

magnetization patterns, radial, Halbach, and axial magnetizations. It should be noted that for Halbach and axial magnetizations, the back iron for the magnets vanishes, $h_{ti} = 0$ or

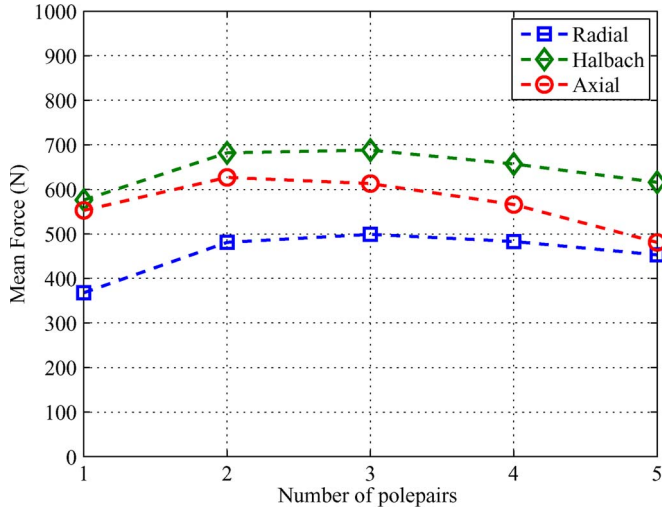


Fig. 12. Mean force level of the optimized interior-magnet topologies for different pole-pair numbers.

$h_{si} = 0$ for interior and exterior magnet, respectively. Modeling of the magnetic field \mathbf{B} inside the air gap is performed using the analytical framework proposed in [6] and [13], hence, end effects of the finite length of the stator and translator are neglected. Calculation of the force is obtained using the Lorentz equation at the center of the air gap and coil region R_{ag}

$$F_{act} = \int_V \mathbf{J} \times \mathbf{B} dV \quad (6)$$

$$= 2\pi R_{ag} \int_0^{L_{act}} J_s B_r dz \Big|_{r=R_{ag}} \quad (7)$$

where $\mathbf{J}_s = h_c \mathbf{J}$ is the surface current density and \mathbf{B}_r is the radial component of the magnetic field at the mean air-gap radius R_{ag} , which is given by

$$R_{ag} = R_t + \frac{g + h_c}{2} \quad \text{for interior magnet} \quad (8)$$

$$R_{ag} = R_t + \frac{g - h_c}{2} \quad \text{for exterior magnet.} \quad (9)$$

Optimization is performed with sequential quadratic programming, where the objective is to maximize the force within the volume and power constraints. The optimization is performed for the three magnetization patterns, for interior- and exterior-magnet topologies, and for different number of pole pairs, $1 \leq N_p \leq 5$.

In Figs. 12 and 13, the force level of the optimized interior-magnet and exterior-magnet topologies are shown, respectively, for different values of the pole-pair number, N_p . It can be observed that for a low pole-pair number, the force levels are relatively low since the saturation level of the back iron (see Table IV) is the limiting constraint. The Halbach magnetization has the highest force levels since no back iron for the magnets is necessary compared with radial magnetization and, hence, a higher magnet height is possible which increases the magnetic

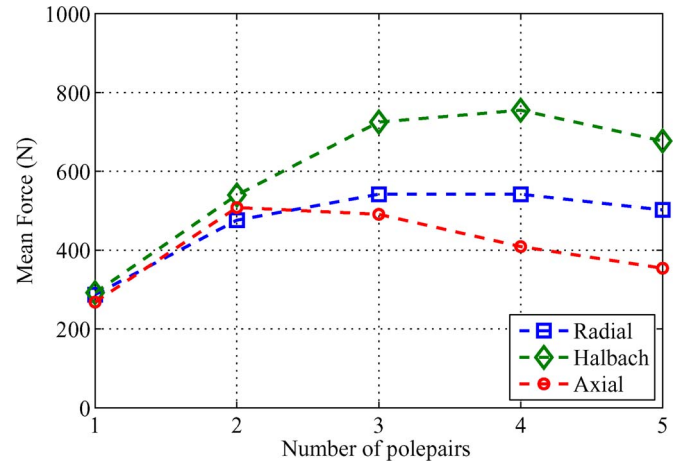


Fig. 13. Mean force level of the optimized exterior-magnet topologies for different pole-pair numbers.

loading \mathbf{B} and, as a result, the force level (6). Compared with axial magnetization, the Halbach magnetization has a higher force level since the magnetic field is concentrated on the air-gap side, and due to the absence of iron pole pieces, it is not limited by saturation levels. Another interesting observation is that for Halbach magnetization, the exterior-magnet topology offers a higher force level compared with the interior-magnet topology since a higher magnet height is possible, increasing \mathbf{B} , while the electrical loading is slightly decreased (due to thermal limitations), which is beneficial considering the total power consumption of the system. Hence, although the allowed copper losses are 50 W less due to thermal limitations, the force level is increased with 67 N. However, this does not hold for axial magnetization since in this case, the flux is not completely focused on the air-gap side, and there is a lot of leakage to the exterior of the actuator (see Fig. 14). The final design is therefore chosen to be an exterior Halbach-magnetized topology with a mean force level of 755 N; the flux density distribution of the full actuator is given in Fig. 15, and the final sizes are given in Table V. The force profile of the final design is checked with a 2-D finite-element analysis (FEA)-simulation and shown in Fig. 16 together with the analytical solution, where the rms current density is 5.1 A/mm². The force-current characteristic is linear up to 4.5 kN, and the necessary rms current density to obtain the peak force of 4 kN is $J_{rms_m} = 25.6$ A/mm².

B. Dynamic Design

In this section, the number of turns N will be determined based upon previously derived current-density levels, speed specifications, and available supply voltages V_{DC} . The losses of the power electronics are neglected as well as the iron losses. The maximum value of the current I_m can be related to the maximum rms current density by

$$I_m = \frac{\sqrt{2} J_{rms_m} S_c}{N P_f} \quad (10)$$

with $S_c = h_c \tau_p / 3$ as the coil area and $P_f = 0.5$ as the packing factor. The EMF e_{ph_N} per turn per phase is calculated with 2-D

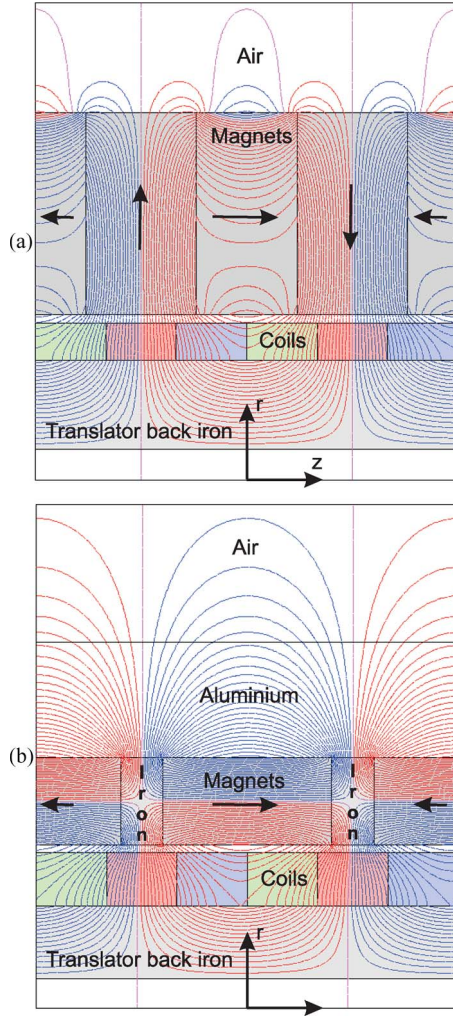


Fig. 14. Flux distribution of (a) the exterior Halbach-magnetized topology and (b) the exterior axial-magnetized topology ($N_p = 4$).

FEA, including end effects at a rated speed of 1 m/s and shown in Fig. 17. From this, the peak EMF is related to the number of turns N and the armature velocity v by

$$E_m = K_{E_N} v N \quad (11)$$

where $K_{E_N} = 1.88 \text{ V} \cdot \text{s/m}$ as observed from Fig. 17. Furthermore, the synchronous inductance per turn is calculated which is $L_{s_N} = 1.9 \text{ } \mu\text{H}$. Therefore, the reactance voltage can be written as

$$\begin{aligned} V_{L_m} &= \omega L_{s_N} N^2 I_m = \frac{\pi v}{\tau_p} L_{s_N} N^2 I_m \\ &= \frac{\sqrt{2} \pi J_{rms_m} S_c v L_{s_N} N}{\tau_p}. \end{aligned} \quad (12)$$

The ohmic voltage drop can be written as

$$V_{R_m} = R_{ph} I_m = \frac{4 \pi R_c \rho N_p}{S_c P_f} N^2 I_m = \frac{4 \sqrt{2} \pi J_{rms_m} R_c \rho N_p N}{P_f} \quad (13)$$

where R_c is the mean radius of the coil, and ρ is the specific resistance. Due to commutation, the stator current is in phase

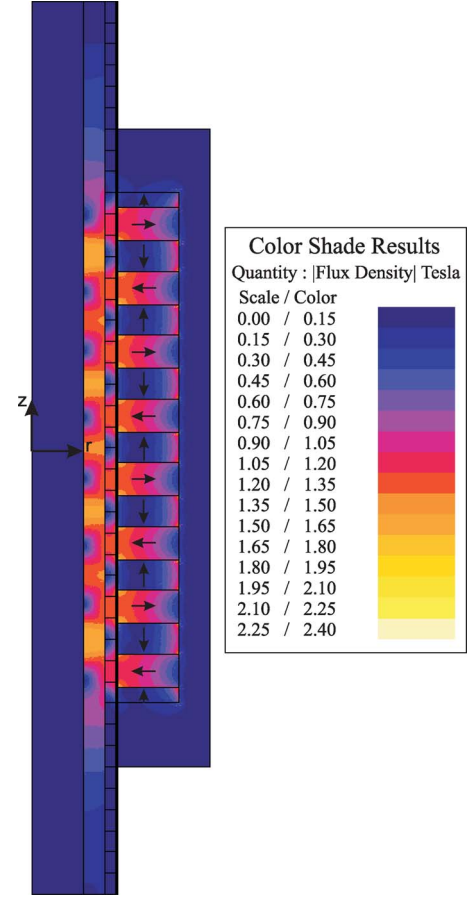


Fig. 15. Flux density in the exterior Halbach-magnetized tubular permanent-magnet actuator.

TABLE V
FINAL DESIGN OF THE EXTERIOR HALBACH-MAGNETIZED
TUBULAR PERMANENT-MAGNET ACTUATOR

Variable	Value
N_p	4
α_p	0.522
τ_p	25.0 mm
h_{ti}	10.5 mm
h_m	24.0 mm
h_c	4.46 mm
J_{rms}	5.10 A/mm ²

with the induced EMF, and, based upon the phasor diagram in the $d-q$ reference frame, the various voltages are related to the phase voltage V_m as

$$V_m^2 = (E_m + V_{R_m})^2 + V_{L_m}^2 \quad (14)$$

where $V_m = V_{DC}/\sqrt{3}$ for space-vector pulsewidth modulation. Considering a dc supply voltage of 14, 42, or 500 V (hybrid vehicle), the number of turns and values of the current are given in Table VI. It can be observed that for the low supply voltages (14 and 42 V), the number of turns is very low due to the limitations on the induced EMF. This results, of course, in extreme high-current values, particularly for obtaining the peak force, which requires expensive power-electronic converters and relatively thick wiring which is not preferred for automotive applications. Therefore, the actuator should

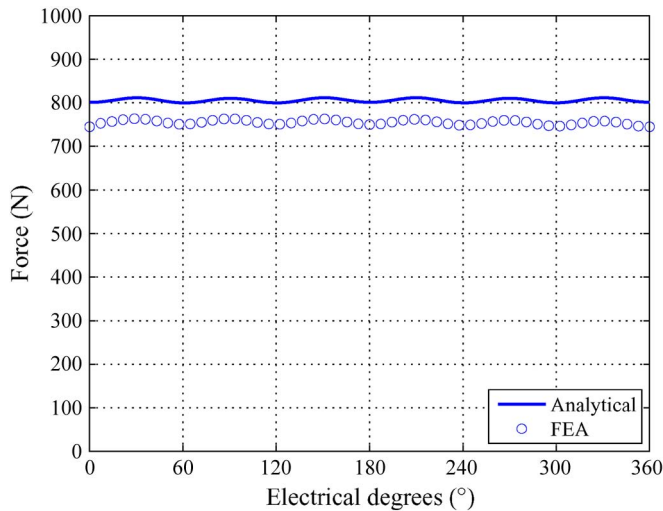


Fig. 16. Force profile of the exterior Halbach-magnetized tubular permanent-magnet actuator.

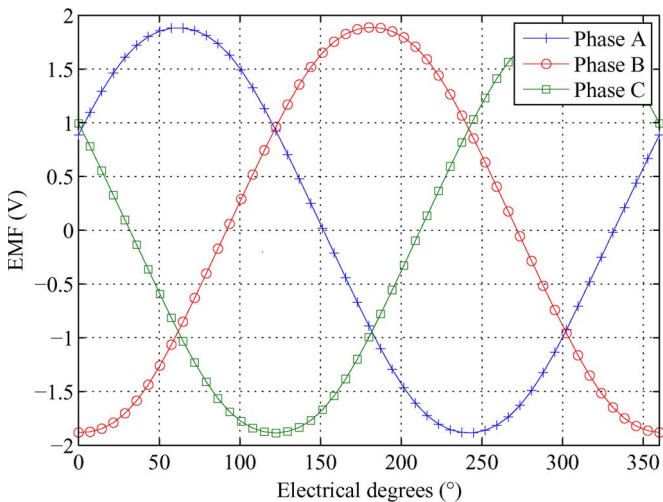


Fig. 17. EMF of the final design of the exterior Halbach-magnetized tubular permanent-magnet actuator at $v = 1$ m/s.

TABLE VI
CIRCUIT PARAMETERS FOR DIFFERENT SUPPLY VOLTAGES

V_{DC}	N	I_{rms} (755 N)	I_{max} (4 kN)	R_{ph}	L_s
14 V	3	126 A	634 A	3.11 m Ω	17.1 μ H
42 V	9	42.1 A	212 A	28.1 m Ω	154 μ H
500 V	114	3.32 A	28.1 A	4.50 Ω	24.7 mH

have a higher force density and perhaps a slotted actuator would be more preferable. However, the low number of turns results in a low inductance and, therefore, a high-bandwidth performance.

VI. CONCLUSION

This paper has described the design aspects for an electromagnetic active suspension system capable of eliminating roll and pitch behavior while maintaining damped behavior of the road vibrations in automotive applications. First, based upon measurements during a test drive on the Nürburgring with a BMW 530 with a passive suspension system, static and dynamic specifications are drawn. The proof of principle

is shown on a quarter-car test setup which mimics the roll and pitch behavior. Comparison of the passive and proposed active electromagnetic suspension system showed the improved performance where a minimization of 94.4% of the passive roll angle is achieved. Since the used electromagnetic suspension system does not meet the volume and mass requirements, an alternative design is proposed. The magnetostatic design is based upon optimization of the static force of a slotless actuator structure for different magnetization topologies as well as for interior- and exterior-magnet solutions. Overall, the Halbach magnetization offers the highest force density where for the given geometry specifications, the exterior Halbach-magnetized topology with four pole pairs is the optimal one. Although it is found that the exterior Halbach magnet topology offers a higher force density compared with the interior one, this does not hold for axial magnetization. Inverting the axial magnetization structure results in a large amount of leakage flux to the exterior of the actuator. The final design is capable of providing a continuous force of 755 N at a maximum speed of 1 m/s which is very close to the obtained specification for active damping. Furthermore, considering the active roll specification, the peak force of 4 kN at 0.1 m/s can be reached; however, the desired rms force of 1 kN cannot be provided since the temperature limit would be exceeded. Due to the low number of turns, a low inductance is obtained which results in a high-bandwidth performance. However, for the low-voltage applications, relatively large currents are necessary which results in expensive power electronic converter and, hence, a slotted actuator with a higher force density is more preferred.

REFERENCES

- [1] R. Rajamani and J. K. Hedrick, "Performance of active automotive suspensions with hydraulic actuators: Theory and experiment," in *Proc. Amer. Control Conf.*, Jun. 1994, vol. 2, pp. 1214–1218.
- [2] Y. M. Sam and K. Hudha, "Modelling and force tracking control of hydraulic actuator for an active suspension," in *Proc. 1st IEEE Conf. Ind. Electron. Appl.*, May 24–26, 2006, pp. 1–6.
- [3] S. Guo, S. Li, and S. Yang, "Semi-active vehicle suspension systems with magnetorheological dampers," in *Proc. IEEE Int. Conf. Veh. Electron. Safety*, Dec. 13–15, 2006, pp. 403–406.
- [4] S. Guo, S. Yang, and C. Pan, "Dynamic modeling of magnetorheological damper behaviors," *J. Intell. Mater. Syst. Struct.*, vol. 17, no. 1, pp. 3–14, 2006.
- [5] Delphi Corporation. [Online]. Available: <http://delphi.com/>
- [6] J. Wang, G. W. Jewell, and D. Howe, "A general framework for the analysis and design of tubular linear permanent magnet machines," *IEEE Trans. Magn.*, vol. 35, no. 3, pp. 1986–2000, May 1999.
- [7] J. Wang, G. W. Jewell, and D. Howe, "Design optimisation and comparison of tubular permanent magnet machine topologies," *Proc. Inst. Elect. Eng.—Elect. Power Appl.*, vol. 148, no. 5, pp. 456–464, Sep. 2001.
- [8] J. J. H. Paulides, L. Encica, E. A. Lomonova, and A. J. A. Vandenput, "Design considerations for a semi-active electromagnetic suspension system," *IEEE Trans. Magn.*, vol. 42, no. 10, pp. 3446–3448, Oct. 2006.
- [9] J. L. G. Janssen, J. J. H. Paulides, E. A. Lomonova, and A. J. A. Vandenput, "Cogging force reduction in tubular permanent magnet actuators," in *Proc. IEEE IEMDC*, May 2007, vol. 1, pp. 266–271.
- [10] J. C. Dixon, *Tires, Suspension and Handling*. Cambridge, U.K.: Cambridge Univ. Press, 1996.
- [11] I. Martins, J. Esteves, G. D. Marques, and F. P. da Silva, "Permanent-magnets linear actuators applicability in automobile active suspensions," *IEEE Trans. Veh. Technol.*, vol. 55, no. 1, pp. 86–94, Jan. 2006.
- [12] California Linear Drives, Inc., *User's Manual Linear Motors*, UM-102 revision B ed., Carlsbad, CA, Nov. 2005.
- [13] J. Wang and D. Howe, "Design optimization of radially magnetized, iron-cored, tubular permanent-magnet machines and drive systems," *IEEE Trans. Magn.*, vol. 40, no. 5, pp. 3262–3277, Sep. 2004.



Bart L. J. Gysen (S'07) was born in Bilzen, Belgium, in 1984. He received the B.Sc. and M.Sc. degrees in electrical engineering from Eindhoven University of Technology, Eindhoven, The Netherlands, where he is currently working toward the Ph.D. degree in the Electromechanics and Power Electronics Group.

His research interest is electromagnetic active-suspension systems for automotive applications.



Johannes J. H. Paulides (M'06) was born in Waalwijk, The Netherlands, in 1976. He received the B.Eng. degree from the Technische Hogeschool 's-Hertogenbosch, The Netherlands, in 1998, and the M.Phil. and Ph.D. degrees in electrical and electronic engineering from the University of Sheffield, Sheffield, U.K., in 2000 and 2005, respectively.

Since 2005, he has been a Research Associate at Eindhoven University of Technology, Eindhoven, The Netherlands, and simultaneously a Director of Paulides BV and Advanced Electromagnetics BV,

small and medium enterprises based in The Netherlands, producing electrical machines and prototype electromagnetic devices. His research activities span all facets of electrical machines, in particular, linear and rotating permanent-magnet-excited machines for automotive and high-precision applications.



Jeroen L. G. Janssen (S'07) was born in Boxmeer, The Netherlands, in 1982. He received the B.Sc. and M.Sc. degrees in electrical engineering from Eindhoven University of Technology, Eindhoven, The Netherlands, where he is currently working toward the Ph.D. degree in the Electromechanics and Power Electronics Group.

His research activities are focused on permanent-magnet-based electromagnetic-vibration isolation for lithographic applications.



Elena A. Lomonova (M'04–SM'07) was born in Moscow, Russia. She received the M.Sc. (*cum laude*) and Ph.D. (*cum laude*) degrees in electromechanical engineering from the Moscow State Aviation Institute (TU), Moscow, Russia, in 1982 and 1993, respectively.

She is currently an Assistant Professor at Eindhoven University of Technology, Eindhoven, The Netherlands. She has worked on electromechanical-actuators design, optimization, and development of advanced mechatronics systems.